In situ analysis of the nucleation of O-and Zn-polar ZnO nanowires using synchrotron-based X-ray diffraction

Valentina Cantelli, Sophie Guillemin, Eirini Sarigiannidou, Francesco Carlá, Bruno Bérini, Jean-Michel Chauveau, Dillon D Fong, Hubert Renevier, Vincent Consonni

▶ **To cite this version:**

Valentina Cantelli, Sophie Guillemin, Eirini Sarigiannidou, Francesco Carlá, Bruno Bérini, et al.. In situ analysis of the nucleation of O-and Zn-polar ZnO nanowires using synchrotron-based X-ray diffraction. Nanoscale, 2022, 14 (3), pp.680-690. ⟨10.1039/D1NR06099F⟩. ⟨hal-03539459⟩

HAL Id: hal-03539459

https://hal.science/hal-03539459v1

Submitted on 21 Jan 2022

HAL is a multi-disciplinary open access archive for the deposit and dissemination of scientific research documents, whether they are published or not. The documents may come from teaching and research institutions in France or abroad, or from public or private research centers.

L'archive ouverte pluridisciplinaire **HAL**, est destinée au dépôt et à la diffusion de documents scientifiques de niveau recherche, publiés ou non, émanant des établissements d'enseignement et de recherche français ou étrangers, des laboratoires publics ou privés.

Copyright - All rights reserved

In situ analysis of the nucleation of O- and Zn-polar ZnO nanowires using synchrotron-based X-ray diffraction

Valentina Cantelli,[1] Sophie Guillemin,[1] Eirini Sarigiannidou,[1] Francesco Carlá,[2] Bruno Bérini,[3] Jean-Michel Chauveau,[3,4] Dillon D. Fong,[5] Hubert Renevier,[1*] and Vincent Consonni.[1*]

[1] *Université Grenoble Alpes, CNRS, Grenoble INP, LMGP, F-38000 Grenoble, France.*

[2] *ESRF, 71 avenue des Martyrs, F-38000 Grenoble France.*

[3] *Université Versailles Saint-Quentin, Université Paris Saclay, CNRS, GEMAC, F-78035 Versailles, France.*

[4] *Université Côte d'Azur, CNRS, CRHEA, Rue Bernard Gregory, F-06560 Valbonne, France.*

[5] *Materials Science Division, Argonne National Laboratory, 9700 S. Cass Ave., Lemont, IL-60439, United States.*

*Corresponding authors: hubert.renevier@grenoble-inp.fr and vincent.consonni@grenoble-inp.fr

Abstract

The selection of the polarity of ZnO nanowires grown by chemical bath deposition offers a great advantage for their integration into a wide variety of engineering devices. However, the nucleation process of ZnO nanowires and its dependence on their polarity is still unknown despite its importance for optimizing their morphology and properties and thus to enhance the related device performances. To tackle this major issue, we combine an *in situ* analysis of the nucleation process of O- and Zn-polar ZnO nanowires on O- and Zn-polar ZnO single crystals, respectively, using synchrotron radiation-based grazing incidence X-ray diffraction with *ex situ* transmission and scanning electron microscopy. We show that the formation of ZnO nanowires obeys three successive phases from the induction, through nucleation to growth phases. The characteristics of each phase, including the nucleation temperature, the shape and dimension of nuclei, as well as their radial and axial development are found to depend on the polarity of ZnO nanowires. A comprehensive description

reporting the dominant physicochemical processes in each phase and their dependence on the polarity of ZnO nanowires is presented, revisiting their formation process step-by-step. These findings provide a deeper understanding of the phenomena at work during the growth of ZnO nanowires by chemical bath deposition and open the perspective to develop a more accurate control of their properties at each step of the process.

Keywords

ZnO nanowires – nucleation & growth – in situ X-ray diffraction – synchrotron radiation

Graphical abstract

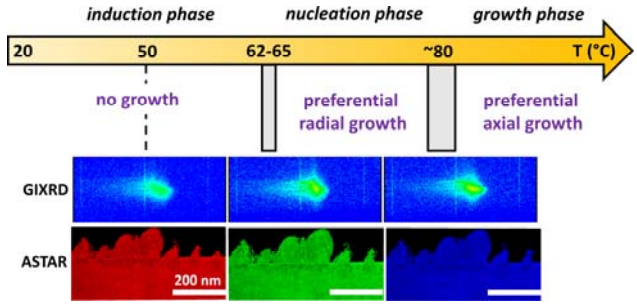

1. Introduction

Owing to its highly anisotropic wurtzite structure,[1] ZnO can spontaneously form arrays of nanowires (NWs) by self-assembly/self-induced growth following a bottom-up approach without need of a foreign catalyst.[2-4] Researchers have demonstrated spontaneous growth along the polar *c*-axis by manifold techniques including physical[5-8] and chemical[9, 10] vapor deposition as well as by wet chemical routes such as electrodeposition[11] and chemical bath deposition (CBD).[12-14] The scalable, low-cost CBD technique operates in a closed reactor heated to relatively low temperatures (70-90 °C), making it compatible with most industrial processes.[12-14] It relies on the heterogeneous formation of ZnO NWs on a dedicated polycrystalline Au[15, 16] or ZnO[17, 18] seed layer in an aqueous solution containing a zinc salt (*e.g.*, zinc nitrate, zinc acetate, zinc sulfate) with a source of hydroxide ions and complexing agents (*e.g.*, sodium hydroxide, ammonia, hexamethylenetetramine (HMTA)).[19, 20] Chemical additives such as polyethylene-imine,[21] chorine ions,[22] citrate ions,[23] and metal nitrate[24-27] have previously been employed to tune the aspect ratio and electronic conductivity. Importantly, the polarity of the NWs can be controlled by the nucleation surface,[28, 29] enabling the formation of O- and Zn-polar ZnO NWs along the $[000\bar{1}]$ and $[0001]$ directions, respectively.[30] This, along with the compatibility of CBD with the fabrication of flexible devices,[31, 32] has made this growth technique highly attractive for a wide range of piezotronic and piezoelectric devices.[33] However, the spontaneous formation mechanism of O- and Zn-polar ZnO NWs has not yet been elucidated, nor has its relationship with crystal polarity. This lack of understanding strongly hinders the ability to precisely control the morphological and structural properties of ZnO NW arrays and inhibits their cost-efficient integration into engineering devices, instead requiring the use of nucleation surfaces pre-patterned by various technological procedures in cleanroom environments.[28, 34-37]

The formation of ZnO NWs grown by CBD is composed of a nucleation phase during which NW nuclei are formed and a subsequent growth phase during which the elongation of the NW nuclei occurs. In contrast to the nucleation phase, the growth phase of ZnO NWs has been extensively investigated, particularly within the past decade.[13, 38-40] The *c*-plane surface area ratio *S*, defined by the area of the top surfaces of all *c*-plane ZnO NWs divided by a given substrate surface area (making it dependent upon both the NW diameter and

density), represents the key parameter for the steady growth phase.[41] The elongation process of ZnO NWs is limited either by i) the surface reaction at the top polar *c*-face for small *S* values, or by ii) the diffusive transport of reactants (*e.g.*, the limiting Zn(II) species) for larger *S* values.[41-44] In the vast majority of cases, a high number density of ZnO NWs on the polycrystalline ZnO seed layer results in large *S* values such that growth occurs in the diffusive transport-limited regime.[41] The diameter and length of ZnO NWs are thus inversely proportional to the number density.[42] In other words, the resulting structural morphology of ZnO NWs, including their dimensions and shape, is entirely governed by the nucleation rate and the processes that take place at the top of the polycrystalline ZnO seed layer. Until recently, all investigations of ZnO NW nucleation, as synthesized by CBD, were conducted *ex situ*, *i.e.*, through the application of characterization techniques after NW formation. It was shown that ZnO NWs nucleate on the surfaces of grains composing the polycrystalline seed layer for typical grain sizes or at the boundaries separating adjacent grains when grain size is much smaller.[45] The vertical alignment of ZnO NWs can be improved by texturing the seed layer along the polar *c*-axis.[17] It was later shown that ZnO NWs mostly nucleate homoepitaxially on polar *c*-axis oriented ZnO grains with either O- or Zn polarity.[46, 47] More recently, ZnO grains oriented with semi-polar planes were also identified as preferential nucleation sites.[48] The O- or Zn-polarity of ZnO grains typically transfers to the ZnO NWs grown on them.[28, 29] Understanding the mechanisms governing the nucleation of ZnO NWs on top of O- and Zn-polar surfaces is important for the NW community, but this has proven difficult to achieve by *ex situ* characterization alone.

Gaining insight into the NW nucleation phase by CBD requires *in situ* characterization of the heterogeneous nucleation process. Such knowledge remains scarce due to the manifold challenges in probing chemical synthesis *in situ* in aqueous solution. Until now, *in situ* experiments have only been performed to investigate the growth phase. McPeak *et al.* used *in situ* X-ray absorption near-edge structure (XANES) spectroscopy to show that ZnO NWs crystallize from $[Zn(H_2O)_6]^{2+}$ species without long-lived intermediates under standard conditions.[49] The same authors also analyzed the role of HMTA by *in situ* attenuated total reflection Fourier transform infrared (ATR-FTIR) spectroscopy.[50] More recently, Rodrigues *et al.* investigated the homogeneous growth process and its relationship with Zn(II) species by *in situ* XANES spectroscopy.[51]

Hsieh *et al.* further studied the development of ZnO nanostructures during the homogeneous growth process using *in situ* transmission electron microscopy (TEM), showing the occurrence of two successive steps in the CBD technique.[52] In order to properly address the issue of the heterogeneous nucleation process by *in situ* X-ray techniques, one challenge is to design a dedicated, leak-tight growth cell that is transparent to X-rays and compatible with a growth medium in aqueous solution.

In the present work, we report results from an *in situ* investigation of the very first steps of the heterogeneous nucleation of ZnO NWs grown by CBD on O- and Zn-polar ZnO single crystals by grazing incidence X-ray diffraction (GIXRD), including in-plane XRD measurements using synchrotron radiation. A dedicated X-ray transparent leak-tight growth cell was designed and used for *in situ* experiments in dynamic conditions where chemical reactants are depleted. In contrast to electron beam probes, the transmission of hard X-rays through water is high and makes them an ideal tool to study the evolution of the morphology and crystallinity of nano-objects in a growth medium in aqueous solution, providing statistically significant datasets over a large population of nuclei. In combination with *ex situ* TEM measurements, the present *in situ* analysis casts light into the nucleation process of ZnO NWs by CBD, affording information on the nucleation temperature, the shape of NW nuclei, their nucleation sites and development, and the dependence of these characteristics on crystal polarity.

2. Experimental details

2.1. Chemical Bath Deposition

O- and Zn-polar ZnO NW nuclei were grown by CBD on commercially available O- and Zn-polar ZnO single crystals (*i.e.*, 5 x 5 mm^2 area, miscut < 0.5° and roughness < 5 Å) from CrysTec GmbH. The ZnO single crystals were annealed under oxygen atmosphere at high temperature to eliminate the residual contaminants and to induce surface reconstructions. The solution of chemical precursors consisted of zinc nitrate hexahydrate [$Zn(NO_3)_2 \cdot 6H_2O$, Sigma-Aldrich] and hexamethylenetetramine [HMTA, Sigma-Aldrich] mixed in an equimolar concentration of 30 mM in ultra-pure water. The investigated growth temperature of 90 °C was reached following a temperature ramp (~5°C / min) for a total growth time of 1 hour.

2.2. Synchrotron-Based X-ray Diffraction

The evolution of the morphological and structural properties of ZnO NW nuclei during CBD on O- and Zn-polar ZnO single crystals was investigated *in situ* by GIXRD using a 20 keV incident beam at D2AM-BM02 beamline[53] of European Synchrotron Radiation Facility (ESRF). Following the cell developed in Ref. [54], an electrochemical flow cell was designed and constructed from polyether ether ketone (PEEK). The leak-tight growth cell consists of a cylindrical X-ray transparent window with a thickness and internal diameter of 90 μm and 7.5 mm, respectively. The cell was connected to upper and lower reservoirs with the same volume, one above and one below the sample. The reservoirs were filled with the solution of chemical precursors and heated with resistive wires (ALOMEGA) protected by polytetrafluoroethylene (PTFE) sheaths. A K-type thermocouple, protected by PTFE sheath and previously calibrated, was placed as close as possible to the sample to record the bath temperature during the experiment. Temperature control was accomplished manually step-by-step. For the GIXRD study, the leak-tight growth cell was installed on the κ-head (kappa-head) of the X-ray goniometer at $\chi = -90°$ (see Fig. 1) with the substrate surface facing down in order to avoid the deposition of precipitated ZnO clusters formed by the homogeneous nucleation process in the solution onto the sample surface. The substrates were kept in place by a vacuum seal to the back of the substrate, made through the sample holder. X-rays reached the substrate surface through the thin PEEK cylindrical window. Due to the height of the window, the maximum out-of-plane exit angle was ~30 °. To minimize X-ray absorption and scattering by the aqueous solution, the samples were located in central position of the leak-tight growth cell, where the internal diameter was smallest (7.5 mm). The S70 2D detector from XPAD™ was placed 90 cm away from the sample. The S70 model only had one module with 120 x 560 pixels and an active surface area equal to 1.5 x 7.5 cm^2. It was characterized by a linear counting rate of 22 x 10^5 photons/s/pixel, a dynamic range of 32 bits, and a pixel size of 130 x 130 μm^2. The 2D detector was mounted perpendicular to the sample surface. Data integration was performed considering a region of interest (ROI) equal to 20 x 140 pixels, corresponding to an angular acceptance equal to 0.165° x 1.16° in the horizontal (i.e. parallel to the sample surface) and vertical (i.e. perpendicular to the sample surface) directions, respectively. The beam size

of 300 µm (H) × 150 µm (V) was defined by the X-ray focusing optics. The horizontal beam divergence, as defined by the focalisation, was equal to 0.017°. Diffraction data were recorded at the incident angle $\alpha_i = 0.12°$, which is slightly smaller than the critical angle for total external reflection at 20 keV for bulk ZnO (α_c = 0.135°). Two types of data were collected during growth: in-plane radial scans, where the modulus of the scattering vector (or momentum transfer) *Q* is varied to allow measurements of NW lattice parameters or strain, and in-plane rocking scans at fixed *Q* length to allow measurements of in-plane size, shape, and mosaicity of the NWs. During the in-plane rocking-scans, the counting time averaged over the ROI barely reached 350 photons/s/pixel with an integration time equal to 0.5s. The 2D detector was kept fixed during the successive in-plane rocking-scans performed as the CBD process proceeded. Reference data were collected for substrate surfaces under dry conditions and after the growth cell was filled with the solution at room temperature (RT). The Ewald sphere construction is shown in Fig. S1 of ESI when the in-plane Bragg condition is fulfilled for the $(11\bar{2}0)$ ZnO lattice planes at 20 keV.

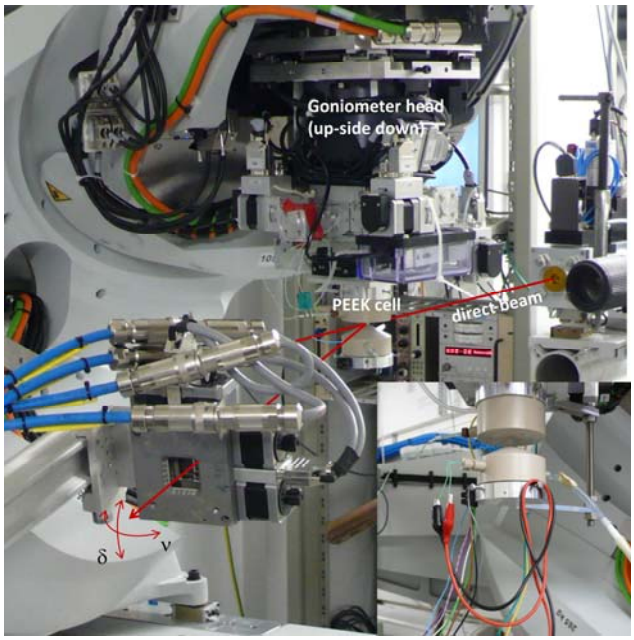

Fig. 1 Picture of the X-ray transparent growth cell mounted on the κ-head of the goniometer of D2AM-BM02 beamline at ESRF at $\chi = -90°$. The substrate surface was placed upside-down with the scattering vector pointed down to the floor. The inset presents a magnification of the growth cell composed of lower and upper reservoirs with the same volume, linked to the X-ray transparent cylindrical tube in which the sample sits.

2.3. Electron Microscopy

The morphology of O- and Zn-polar ZnO single crystal substrates was investigated by atomic force microscopy (AFM) using a BRUKER Dimension ICON instrument in PeakForce tapping mode. A silicon tip (Bruker ScanAsyst Air model) with a 0.4 N/m spring constant and a nominal tip radius of 2 nm was used with a resolution of 512 pixels x 512 pixels. The structural properties of ZnO nuclei were investigated by field-emission scanning electron microscopy (FESEM) using a ZEISS Ultra+ microscope and by TEM using a JEOL-JEM 2010 microscope operating at 200 kV with a 0.19 nm point-to-point resolution. High-angle annular dark field (HAADF) imaging, and automated crystalline orientation and phase mapping (ACOM) were collected by scanning TEM (STEM) with a JEOL 2100F FEG microscope operating at 200 kV with a 0.2 nm resolution in the scanning mode. The STEM instrument was further equipped with a precession electron beam diffraction module provided by NanoMEGAS. The precession angle in our experiments was 1.2°. The combination of the precession module with ACOM-TEM is usually referred to as ASTAR. All the TEM specimens were prepared by focused-ion beam (FIB) in a Zeiss NVision40 SEM-FIB microscope.

3. Results

The leak-tight growth cell was designed to work in the most widely used CBD configuration, namely under dynamic conditions where the depletion of chemical reactants with time occurs.[43] In that configuration, neither continuous flow to introduce the chemical reactants nor mechanical stirring during the CBD process were used. The nucleation and formation of ZnO NWs thus operated in the well-known framework of the surface reaction- / diffusive transport-limited regimes.[41] Prior to the experiments in large-scale facilities, the working of the leak-tight growth cell was assessed in lab-scale facilities by performing the CBD over a typical *c*-axis oriented polycrystalline ZnO seed layer deposited by dip coating under the same conditions. As presented in Fig. S2, vertically aligned ZnO NWs are formed on a typical *c*-axis oriented polycrystalline ZnO seed layer, showing the relevance of using the designed leak-tight growth cell to investigate in detail the CBD of ZnO NWs.

The evolution of the morphology of ZnO nuclei grown on the O- and Zn-polar ZnO single crystals was monitored *in situ* by in-plane XRD measurements. In-plane rocking scans across the $11\bar{2}0$ Bragg reflections

are presented in Fig. 2(a-b) along with the corresponding images of the 2D detector in Fig. 2(c-h). The raw data for the radial scans are not shown here.

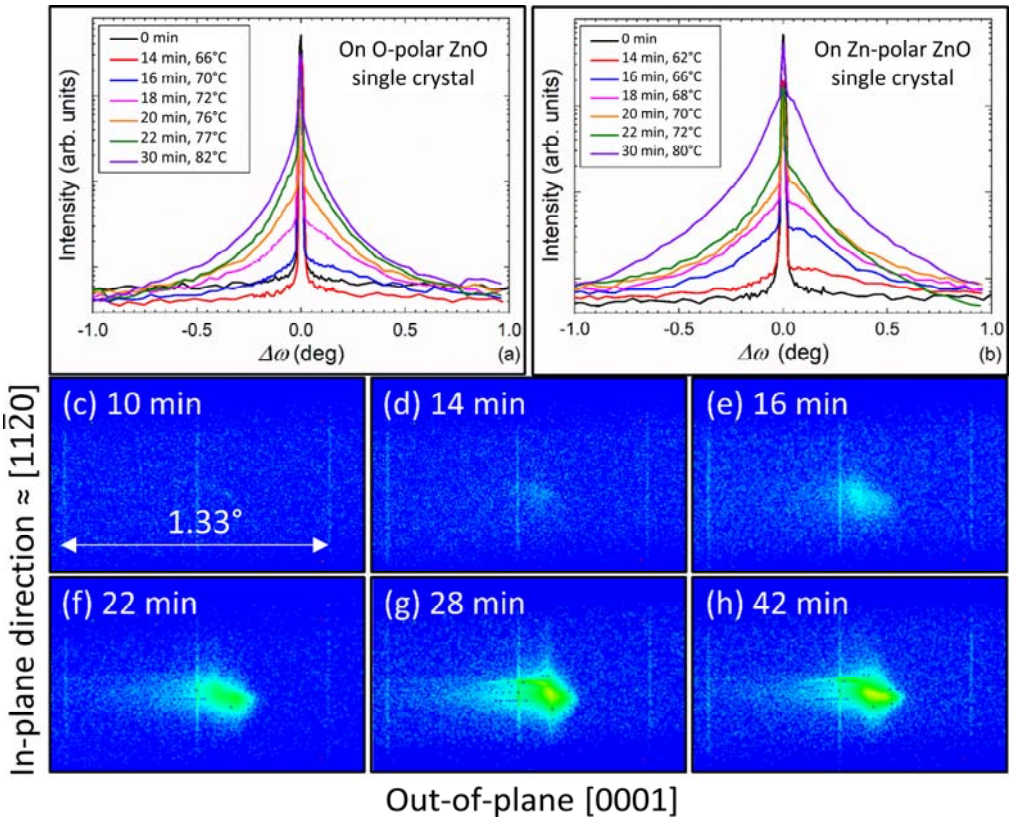

Fig. 2 In-plane rocking scans collected across the 11$\bar{2}$0 Bragg reflection during the formation of ZnO nuclei grown on the (a) O- and (b) Zn-polar ZnO single crystals, respectively. The data plotted in logarithmic scale were extracted from the integration in the ROI of the scattered intensity recorded on the 2D detector. (c-h) Images of the 2D detector obtained slightly off the (11$\bar{2}$0) ZnO substrate Bragg condition (*i.e.*, $\Delta\omega = \pm 0.032°$) for a series of growth times in the case of ZnO nuclei grown on the Zn-polar ZnO single crystals. The data are plotted in logarithmic scale. Note that the images are rotated by 90° and hence the in-plane direction is parallel to the sample and the out-of-plane direction corresponds to the scattering vector component Q_z. The very thin vertical streaks correspond to the presence of double pixels at the edge of the module chips. The distance in between two streaks is equal to 160 pixels (*i.e.*, 1.33°). The tails on the left side of the main scattered intensity spot in (f-h) extend along the out-of-plane direction and originate from the intersection of the (11$\bar{2}$0) ZnO rod with the Ewald sphere while scanning the ω-angle.

At a growth time of 0 min (*i.e.*, at room temperature), sharp Bragg peaks originating from the O- and Zn-polar ZnO single crystals are revealed and indicate their high crystalline quality. For growth times shorter than 13

(resp. 14 min) in the case of growth on O-polar (resp. Zn-polar) ZnO single crystal, no significant evolution of the characteristic Bragg peak is observed, as shown in Fig. 2(a,b,c). At a growth time of 14-16 min, a diffuse scattering close to the ZnO Bragg peak can be observed in Fig. 2(a,b,d), indicating the nucleation of stable ZnO islands on the O- and Zn-polar ZnO single crystals. The finite in-plane size of the stable ZnO nuclei is responsible for the apparent broadening of the Bragg peak, and the Bragg peaks exhibit both sharp and broad components, as shown in Fig. 2(a,b). Once the heterogeneous nucleation process begins, the development of stable ZnO nuclei is fast and evolves during the 2 minutes needed for recording a single curve, accounting for the asymmetry of the diffuse scattering at the early stages of growth. The higher degree of asymmetry on the Zn-polar ZnO single crystal further suggests that ZnO nuclei develop faster on that surface. According to the data, the nucleation temperature for growth on the O-polar ZnO single crystal is ~65 °C while for growth on the Zn-polar ZnO single crystal is ~62 °C. The heterogeneous nucleation process of ZnO nuclei thus starts at a slightly lower temperature on the Zn-polar ZnO single crystal than on the O-polar ZnO single crystal, which is due to some peculiarities in the nucleation process itself.

In order to determine the FWHM values from Fig. 2(a,b), the rocking-scan curves were fitted with Pearson7 functions using Fityk 1.2.1 software.[55] The in-plane size $\langle D \rangle$ of the nucleus in the $[1\bar{1}00]$ direction was calculated by the following formula:

$$\frac{1}{\langle D \rangle} = Q(11\bar{2}0) \times \Delta\omega_{FWHM} = \frac{2\sin\theta}{\lambda} \times \Delta\omega_{FWHM} = \frac{\Delta\omega_{FWHM}}{d_{11\bar{2}0}} \quad (1)$$

where $Q(11\bar{2}0) = \frac{2}{a}$ and $\Delta\omega_{FWHM}$ is the FWHM of the in-plane rocking scans. The evolution of the in-plane size $\langle D \rangle$ of ZnO nuclei grown on the O- and Zn-polar ZnO single crystals can be determined as a function of the growth time and temperature and is reported in Fig. 3(a-b).

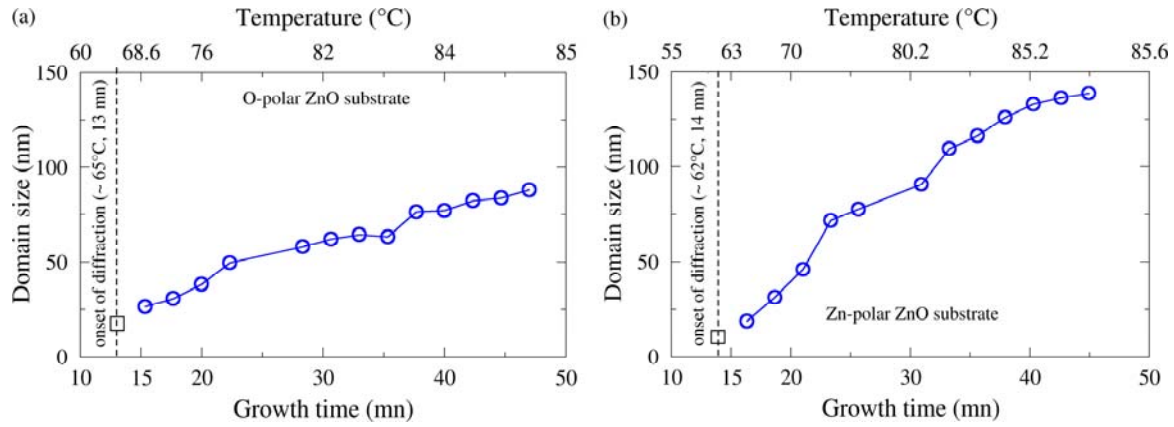

Fig. 3 Evolution of the in-plane size of ZnO nuclei grown on the (a) O- and (b) Zn-polar ZnO single crystals, respectively, as a function of the growth time and temperature. The values of the in-plane size were deduced from the FWHMs of the Bragg peaks in the in-plane rocking scans presented in Fig. 2.

Once the heterogeneous nucleation process has started, a gradual increase in the in-plane size of ZnO nuclei grown on the O-polar single crystal is observed from about 17 nm (extrapolated value at 13 min) to 90 nm as the growth time is increased from 13 to 47 min. The in-plane growth rate is fairly constant in this regime, indicating the steady development of ZnO nuclei on the surface of O-polar ZnO single crystal. In contrast, the increase in the in-plane size of ZnO nuclei grown on the Zn-polar ZnO single crystal is larger and proceeds from 11 nm (extrapolated value at 14 min) to 140 nm as the growth time is increased from 14 to 45 min. The in-plane growth rate is thus higher but exhibits two successive regimes: an initial, steady development of ZnO nuclei in the plane of growth occurs from 14 to about 35 min, followed by a progressive, slower development from a growth time of 45 min. The transition in the regime takes place at an in-plane size close to 125 nm. The development of ZnO nuclei during the initial stage is thus much faster on the Zn-polar ZnO single crystal than on the O-polar ZnO single crystal, and exhibits two successive regimes in the time-dependent in-plane growth rate. Concomitantly, the integrated intensity of the Bragg peak coming from ZnO nuclei on ZnO single crystals with either polarity significantly increases. These in-plane XRD measurements further reveal that the ZnO nuclei are homoepitaxial with the O- and Zn-polar ZnO single crystals since no difference between the azimuth angles of the substrate and of the nuclei is detected.

After the experiment, the samples were removed from the solution in the leak-tight growth cell, rinsed with deionized water, and dried with nitrogen flow. TEM and FESEM imaging were performed *ex situ* to complement the structural analysis through the determination of the morphology and orientation of ZnO nuclei. TEM and high-resolution TEM images of ZnO nuclei grown on the O- and Zn-polar ZnO single crystals are presented in Fig. 4 along with ASTAR measurements revealing their crystalline phase and orientation.

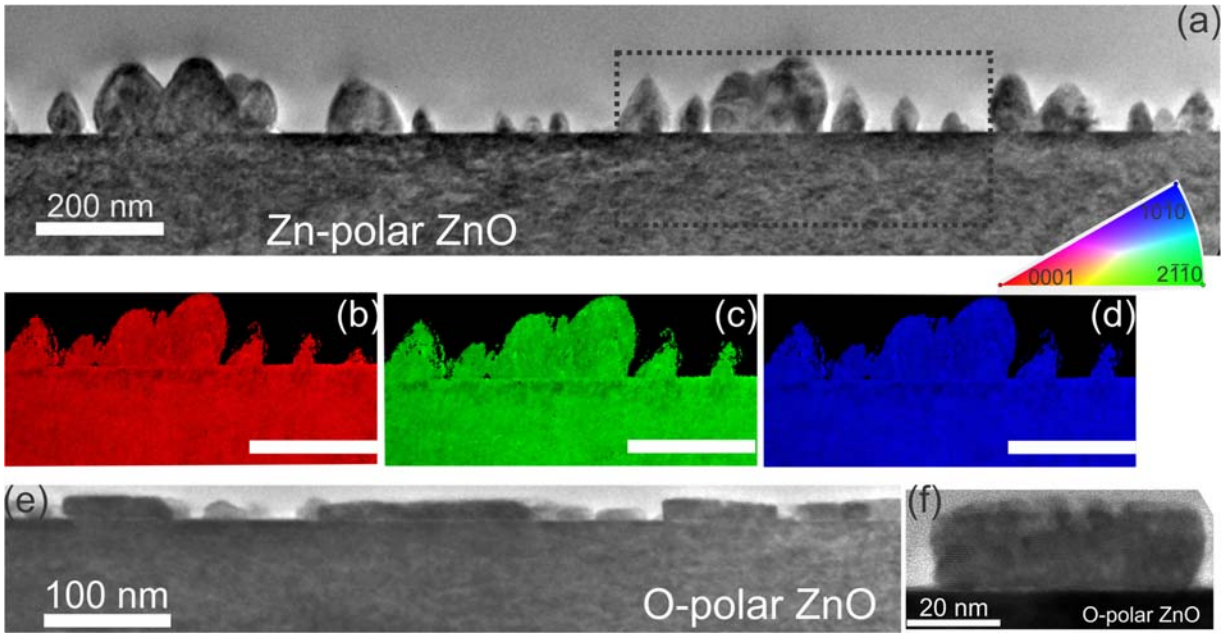

Fig. 4 (a) Low magnification TEM image of ZnO nuclei grown on the Zn-polar ZnO single crystal along the $\langle 01\bar{1}0 \rangle$ zone axis. ASTAR maps collected in the rectangular area representing the crystal orientation (b) along the $\langle 0001 \rangle$ growth direction and (c,d) along the perpendicular $\langle 2\bar{1}\bar{1}0 \rangle$ and $\langle 10\bar{1}0 \rangle$ directions, respectively. The color scale is given as an inset. The scale bar denotes 200 nm. (e) Low magnification TEM image of ZnO nuclei grown on the O-polar ZnO single crystal along the $\langle 2\bar{1}\bar{1}0 \rangle$ zone axis. (f) High-resolution TEM image of a ZnO nucleus grown on the O-polar ZnO single crystal.

The cross-sectional TEM images of ZnO nuclei grown on the O- and Zn-polar ZnO single crystals indicate several striking differences regarding their shape and size. ZnO nuclei grown on the Zn-polar ZnO single crystal exhibit an elongated shape marked by the formation of inclined facets with a mean tilt angle that is often close to 73° (or 107 °), corresponding to the $(2\bar{1}\bar{1}1)$ planes, as seen in Fig. 4a. Other ZnO nuclei present the formation of inclined facets with a mean tilt angle close to 90°, corresponding to the non-polar *m*-planes.

The mean in-plane diameter of ZnO nuclei grown on the Zn-polar ZnO single crystal is 66 ± 27 nm. Their mean out-of-plane length is larger and equal to 72 ± 25 nm. The aspect ratio of ZnO nuclei grown on the Zn-polar ZnO single crystal is therefore higher than 1, exhibiting an elongated shape that is fairly similar to the NW shape. In contrast, ZnO nuclei grown on the O-polar ZnO single crystal exhibit a platelet shape marked by the systematic formation of perpendicular facets corresponding to the low energy non-polar *m*-planes, as seen in Fig. 4e-f. The mean in-plane diameter of ZnO nuclei grown on the O-polar ZnO single crystal lies in the range of several tens of nanometers. However, their mean out-of-plane length is smaller and equal to 17 ± 2 nm. The aspect ratio of ZnO nuclei grown on the O-polar ZnO single crystal is consequently lower than 1, accounting for their platelet shape.

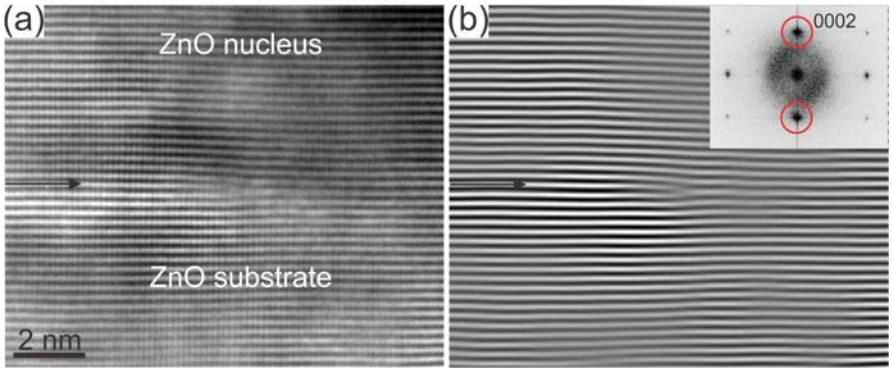

Fig. 5 (a) High-resolution TEM image of the interface region between the ZnO nucleus and the Zn-polar ZnO single crystal. The arrow denotes the interface. (b) Corresponding 0002 Bragg image of the interface area through the use of a mask on the 0002 spatial frequencies to reveal only the (0002) planes. The inset shows the electron diffraction pattern with the 0002 peaks circled.

Two typical high-resolution TEM images recorded at the interface between a ZnO nucleus and the Zn- and O-polar ZnO single crystals are presented in Figs. 5 and 6, respectively. The homoepitaxial relationship of the ZnO nucleus with the Zn-polar ZnO single crystal is shown by ASTAR maps in Fig. 4b-d and by the electron diffraction pattern in the inset of Fig. 5b. The homoepitaxial relationship of the ZnO nucleus with the O-polar ZnO single crystal is shown by the fast Fourier transform (FFT) image in Fig. 6b. Additionally, the interface analysis between the ZnO nuclei and the Zn- and O-polar ZnO single crystals using TEM imaging generally shows that an atomic step occurs. As an example, the presence of an atomic step is clearly indicated at the

interface between the ZnO nucleus and the Zn-polar ZnO single crystal in Fig. 5a. This indicates that the ZnO nuclei preferentially form on defects such as surface steps.

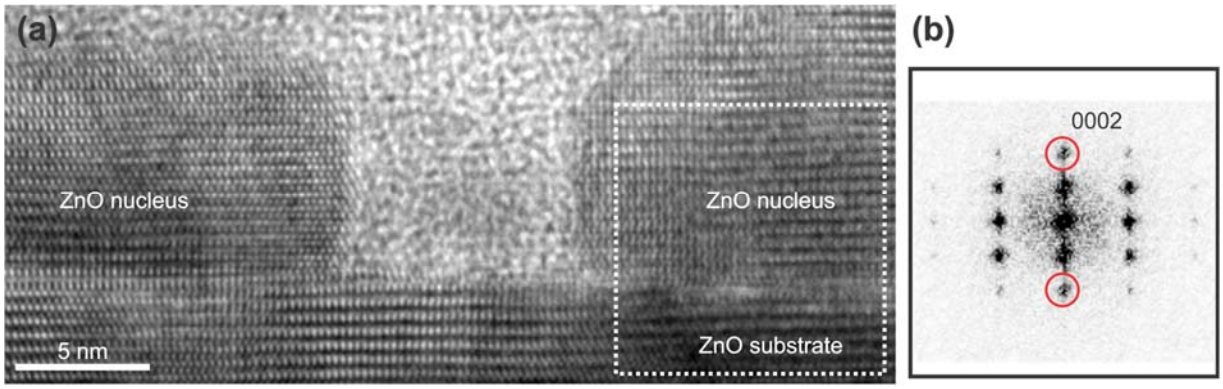

Fig. 6 (a) High-resolution TEM image of the interface region between the ZnO nuclei and the O-polar ZnO single crystal. (b) Corresponding FFT image of the dotted rectangular area in (a).

Interestingly, the formation of ZnO nuclei on the Zn-polar ZnO single crystal is aligned along a specific direction corresponding to the straight surface steps formed after thermal annealing, as presented in Fig. 7a,c. In contrast, the formation of ZnO nuclei on the O-polar ZnO single crystal does not exhibit a clear alignment along a specific direction, which is consistent with the presence of round-shaped surface steps along with the straight surface steps formed after thermal annealing, as revealed in Fig. 7b,d. These strongly support the preferential formation of ZnO nuclei on defects at the surfaces of O- and Zn-polar ZnO single crystals. Furthermore, the mean diameter of ZnO nuclei is larger on the Zn-polar ZnO single crystal than on the O-polar ZnO single crystal, but they have a similar order of magnitude, as determined from *in situ* GIXRD measurements. The dispersion of sizes of ZnO nuclei is however higher on the Zn-polar ZnO single crystal than on the O-polar ZnO single crystal.

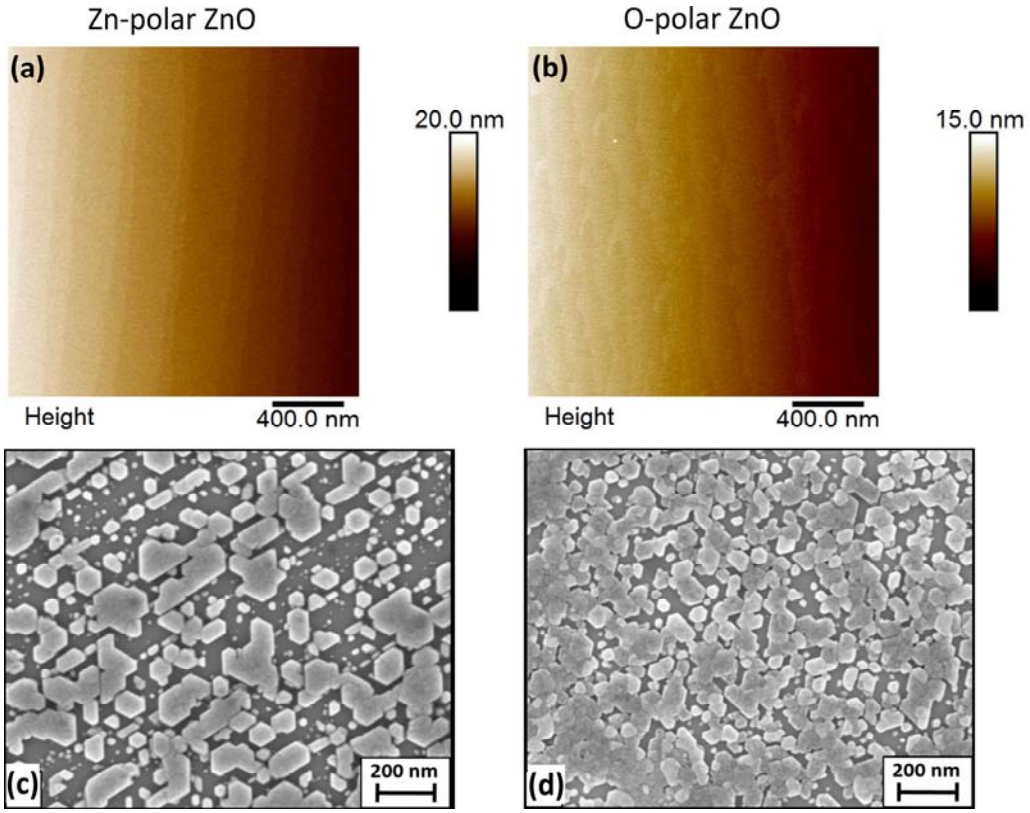

Fig. 7 Top-view AFM images showing the topography of (a) Zn-polar and (b) O-polar ZnO single crystals. Top-view FESEM images of ZnO nuclei grown on the (c) Zn-polar and (d) O-polar ZnO single crystals.

4. Discussion

The experimental data collected here, and the combination of *in situ* / *ex situ* analysis, shines a new light on the nucleation process of ZnO NWs and its dependence on the polarity of ZnO single crystals. A schematic diagram recapitulating the comprehensive description of the formation process of O- and Zn-polar ZnO NWs on O- and Zn-polar ZnO single crystals is presented in Fig. 8.

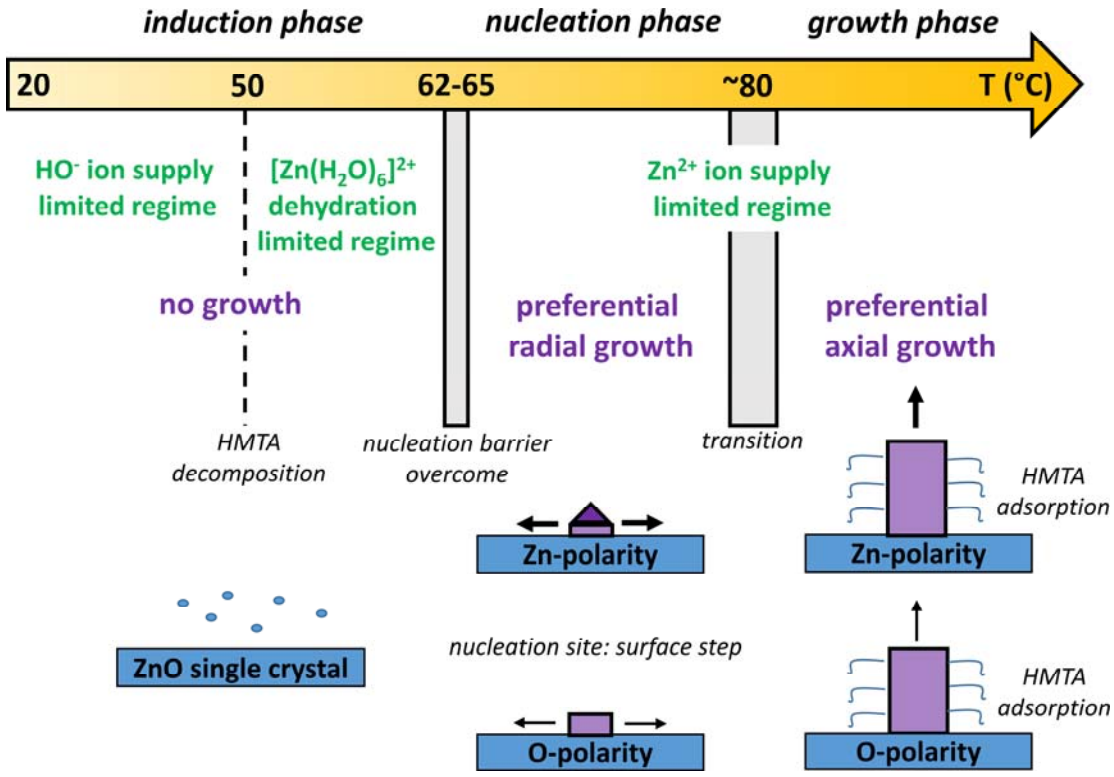

Fig. 8 Schematic diagram describing the dominant physicochemical processes during the three phases of the formation of O- and Zn-polar ZnO NWs by CBD on O- and Zn-polar ZnO single crystals, respectively.

Three successive phases have been established for the formation process of O- and Zn-polar ZnO NWs on the O- and Zn-polar ZnO single crystals, respectively. The development of ZnO nuclei and NWs through the nucleation and growth phases is governed by the following set of chemical reactions:[3, 19, 20]

$$Zn(NO_3)_2 \longrightarrow Zn^{2+} + 2NO_3^- \quad (2)$$

$$(CH_2)_6N_4 + 6H_2O \longrightarrow 6HCHO + 4NH_3 \quad (3)$$

$$NH_3 + H_2O \rightleftharpoons NH_4^+ + OH^- \quad (4)$$

$$Zn^{2+} + 2OH^- \rightleftharpoons ZnO_{(s)} + H_2O \quad (5)$$

$$Zn^{2+} + 6\,H_2O \rightleftharpoons [Zn(H_2O)_6]^{2+} \quad (6)$$

The first phase occurs when the growth temperature is raised from room temperature to 62 and 65 °C on the Zn- and O-polar ZnO single crystals, respectively, and corresponds to the induction phase during which the supersaturated solution remains in a metastable equilibrium.[56] In that phase, only the formation of ZnO nuclei

with subcritical size occurs on the surface of ZnO single crystals. The first phase can be split into two successive regimes, during which the nucleation process on the surface of ZnO single crystals does not initiate for different reasons. While the solubilization of $Zn(NO_3)_2$ occurs at room temperature to produce Zn^{2+} ions at the low pH of 5.5. (Eq. 2),[14, 40] the decomposition of HMTA molecules is thermally activated to produce HO^- ions *via* the hydrolysis of NH_3 (Eqs. 3-4).[39, 49, 57, 58] The main chemical reaction involving Zn^{2+} ions and HO^- ions to crystallize ZnO (Eq. 5) is thus driven kinetically by the pH-dependent thermal decomposition of HMTA molecules,[39] which is known to start at about 50 °C.[59] In other words, HO^- ions act as the limiting species during the first regime of that phase, namely when the growth temperature is raised from room temperature to about 50 °C.[60] This contrasts with the subsequent regimes and phases describing the formation of O- and Zn-polar ZnO NWs, during which the Zn^{2+} ions become the limiting species with respect to highly mobile and abundant HO^- ions in water following the efficient decomposition of HMTA molecules at higher temperature.[41, 43] The second regime of the first phase occurs when the growth temperature is raised from about 50 to 62-65 °C. Here, as the growth temperature is higher, the decomposition of HMTA molecules is more efficient, releasing greater amounts of highly mobile HO^- ions in water and attaining a faster growth front.[41, 43] HO^- ions are no longer the limiting species during the second regime of that phase. Importantly, it is well-known that the coordination of Zn^{2+} ions with water molecules in aqueous solution is octahedral, through the formation of $[Zn(H_2O)_6]^{2+}$ ions as shown by molecular dynamics simulations,[61] XRD,[62] and X-ray absorption spectroscopy[63] measurements (Eq. 6). The behaviour of Zn^{2+} ions in aqueous solution is comparable to the behaviour of many metal ions binding H_2O molecules through ionic bonds with electrostatic character.[64] The crystallization of ZnO is thus direct, but takes place through the thermally-activated dehydration process of $[Zn(H_2O)_6]^{2+}$ ions and subsequent incorporation of zinc atoms at the growth front,[41, 49] for which a significant energy barrier of 198 ± 24 kJ/mol needs to be overcome.[43] The second phase proceeds when the nucleation temperature of about 62 and 65 °C on the respective Zn- and O-polar single crystals is reached, overcoming the energy barrier for nucleation. It corresponds to the nucleation phase during which the very first ZnO nuclei with critical size or larger are formed, preferentially on the surface steps where the nucleation energy barrier is lower. In the second phase, the limiting species switches from HO^- ions to Zn^{2+} ions. Very interestingly, the

lower nucleation temperature of ZnO nuclei on the Zn-polar ZnO single crystals can be explained by the larger surface reactivity of the Zn-polar *c*-planes in aqueous solution, notably with H_2O molecules,[65, 66] rather than by the larger number density of surface defects.[67] The surface energy of the Zn-polar *c*-plane is higher than the surface energy of the O-polar *c*-plane, leading to larger instability and activity with many reactants.[65] The Zn-polar surface has been found to be highly reactive for the dissociation of H_2O molecules on the zinc atoms at room temperature, while the O-polar surface requires the presence of oxygen vacancies to activate that dissociation process through an endothermic reaction.[66] In other words, the dehydration process of the $[Zn(H_2O)_6]^{2+}$ ions required to incorporate zinc atoms and crystallize ZnO[41, 43, 49] can be assisted by the surface and is certainly more efficient on the Zn-polar ZnO single crystals than on the O-polar ZnO single crystals, explaining the dependence of the nucleation temperature on the polarity. More generally, when a polycrystalline ZnO seed layer is used, the nucleation of ZnO NWs has been shown to occur on the surfaces of grains,[45, 46] but it is likely that the preferential nucleation sites involve a defect at the surface of each grain such as a surface step. This may account for the nucleation of ZnO NWs on top of particular *c*-axis oriented grains and not on all the *c*-axis oriented grains composing the polycrystalline ZnO seed layer.[46] Once the heterogeneous nucleation process has been initiated during the second phase, the radial development of stable ZnO nuclei is fast, but it is faster on the Zn-polar ZnO single crystals than on the O-polar ZnO single crystals.[68] More importantly, the ZnO nuclei with the O-polarity when grown on the O-polar ZnO single crystal[28] exhibit a flat top surface, which is explained by the low surface energy of the O-polar *c*-plane.[65] In contrast, the ZnO nuclei with the Zn-polarity when grown on the Zn-polar ZnO single crystal[28] present a flat surface with a much smaller area owing to the higher surface energy of the Zn-polar *c*-plane[65] along with some inclined semi-polar facets with an intermediate energy in the wurtzite structure[69] for their stabilization. The presence of semi-polar facets at the top of ZnO nuclei with the Zn-polarity is responsible for their larger radial development as they are more reactive than the non-polar *m*-planes. The axial development of stable ZnO nuclei is consequently reduced strongly during the nucleation phase. As the growth temperature continues to increase, the third phase occurs and corresponds to the growth phase of ZnO nuclei during which they elongate along the polar *c*-axis. The radial development of ZnO nuclei during the nucleation phase is mostly replaced by the axial elongation

of ZnO NWs during the growth phase. HMTA molecules are well-known to inhibit the development of the non-polar *m*-plane sidewalls of ZnO NWs through their adsorption process as capping agents.[57, 58, 70] The larger number of dangling bonds on the Zn-polar top surface than on the O-polar top surface is also favourable for the more efficient incorporation of zinc atoms and thus for the larger axial growth rate of Zn-polar ZnO NWs as compared to O-polar ZnO NWs.[68] The present comprehensive description indicates that the deeper knowledge and control of the nucleation phase of O- and Zn-polar ZnO NWs grown by CBD opens many perspectives to thoroughly optimize their morphological and structural properties for a large number of optoelectronic[71-73] and piezoelectric[33, 74] devices. In particular, considering the effect of the polarity of ZnO NWs on the physicochemical processes at work during their formation offers a great opportunity to boost the performance of the related engineering devices.[33]

5. Conclusions

In summary, we have combined an *in situ* analysis of the nucleation process of O- and Zn-polar ZnO NWs grown by CBD on O- and Zn-polar ZnO single crystals, respectively, using synchrotron radiation-based GIXRD measurements with *ex situ* TEM and FESEM imaging in different modes. A dedicated leak-tight growth cell transparent to X-rays has been built for that purpose. The formation of ZnO NWs is found to follow three successive phases from the induction, through nucleation to growth phases. The characteristics of each phase, including the nucleation temperature, the shape and dimension of nuclei, as well as their radial and axial development has been discussed in detail along with their dependence on the polarity of ZnO NWs. A comprehensive description highlighting the dominant physicochemical processes in each phase has been established and its dependence on the polarity of ZnO NWs has been taken into account. The present findings open many perspectives to more carefully control the development of ZnO NWs by CBD at each step of the formation process.

Data availability statements

The data that support the findings of this study are available from the corresponding authors upon reasonable request.

Conflicts of interest

The authors declare no conflicts of interest.

Acknowledgements

The authors acknowledge the financial support from the French National Research Agency through the projects ROLLER (ANR-17-CE09-0033) and DOSETTE (ANR-17-CE24-0003). V. Cantelli was supported by the Nanosciences Foundation, and D.D.F. was supported by both an award from the Nanosciences Foundation and the U.S. Department of Energy (DOE), Office of Science, Office of Basic Energy Sciences, Materials Sciences and Engineering Division. The authors thank the French CRG and SOLEIL committee for beamtime allocation (proposal number 20130642) and facilities placed at our disposal at beamline BM2-D2AM of the ESRF, and in particular S. Arnaud, N. Blanc, and N. Boudet for their help with the experimental setup. This work has further benefited from some of the characterization equipments of the Grenoble INP – CMTC platform supported by the LabEx CEMAM under the contract ANR-10-LABX-44-01. The authors thank Gilles Renou, Grenoble, France, for his assistance in the acquisition of ASTAR maps.

References

1. U. Ozgur, Y. I. Alivov, C. Liu, A. Teke, M. A. Reshchikov, S. Dogan, V. Avrutin, S. J. Cho and H. Morkoc, *J. Appl. Phys.*, 2005, **98**, 103.
2. Z. L. Wang, *J. Phys.-Condens. Matter*, 2004, **16**, R829-R858.
3. L. Schmidt-Mende and J. L. MacManus-Driscoll, *Mater. Today*, 2007, **10**, 40-48.
4. Y. Y. Zhang, M. K. Ram, E. K. Stefanakos and D. Y. Goswami, *J. Nanomater.*, 2012, **2012**, 22.
5. B. D. Yao, Y. F. Chan and N. Wang, *Appl. Phys. Lett.*, 2002, **81**, 757-759.
6. S. C. Lyu, Y. Zhang, C. J. Lee, H. Ruh and H. J. Lee, *Chem. Mater.*, 2003, **15**, 3294-3299.
7. Y. Sun, G. M. Fuge and M. N. R. Ashfold, *Chem. Phys. Lett.*, 2004, **396**, 21-26.
8. T. Nobis, E. M. Kaidashev, A. Rahm, M. Lorenz, J. Lenzner and M. Grundmann, *Nano Lett.*, 2004, **4**, 797-800.
9. J. J. Wu and S. C. Liu, *Adv. Mater.*, 2002, **14**, 215-+.
10. W. I. Park, G. C. Yi, M. Y. Kim and S. J. Pennycook, *Adv. Mater.*, 2002, **14**, 1841-1843.
11. S. Peulon and D. Lincot, *Adv. Mater.*, 1996, **8**, 166-170.
12. L. Vayssieres, K. Keis, S. E. Lindquist and A. Hagfeldt, *J. Phys. Chem. B*, 2001, **105**, 3350-3352.
13. L. Vayssieres, *Adv. Mater.*, 2003, **15**, 464-466.
14. S. Yamabi and H. Imai, *J. Mater. Chem.*, 2002, **12**, 3773-3778.
15. S. Xu, C. Lao, B. Weintraub and Z. L. Wang, *J. Mater. Res.*, 2008, **23**, 2072-2077.
16. C. Lausecker, B. Salem, X. Baillin, H. Roussel, E. Sarigiannidou, F. Bassani, E. Appert, S. Labau and V. Consonni, *Nanotechnol.*, 2019, **30**, 11.
17. L. E. Greene, M. Law, D. H. Tan, M. Montano, J. Goldberger, G. Somorjai and P. D. Yang, *Nano Lett.*, 2005, **5**, 1231-1236.
18. J. Song and S. Lim, *J. Phys. Chem. C*, 2007, **111**, 596-600.
19. D. Lincot, *MRS Bull.*, 2010, **35**, 778-789.
20. S. Xu and Z. L. Wang, *Nano Res.*, 2011, **4**, 1013-1098.
21. L. E. Greene, B. D. Yuhas, M. Law, D. Zitoun and P. D. Yang, *Inorg. Chem.*, 2006, **45**, 7535-7543.
22. L. Xu, Y. Guo, Q. Liao, J. Zhang and D. Xu, *J. Phys. Chem. B*, 2005, **109**, 13519-13522.
23. J. H. Kim, D. Andeen and F. F. Lange, *Adv. Mater.*, 2006, **18**, 2453-2457.
24. J. Joo, B. Y. Chow, M. Prakash, E. S. Boyden and J. M. Jacobson, *Nat. Mater.*, 2011, **10**, 596-601.
25. C. Verrier, E. Appert, O. Chaix-Pluchery, L. Rapenne, Q. Rafhay, A. Kaminski-Cachopo and V. Consonni, *Inorg. Chem.*, 2017, **56**, 13111-13122.
26. P. Gaffuri, E. Appert, O. Chaix-Pluchery, L. Rapenne, M. Salaun and V. Consonni, *Inorg. Chem.*, 2019, **58**, 10269-10279.
27. C. Lausecker, B. Salem, X. Baillin, O. Chaix-Pluchery, H. Roussel, S. Labau, B. Pelissier, E. Appert and V. Consonni, *Inorg. Chem.*, 2021, **60**, 1612-1623.
28. V. Consonni, E. Sarigiannidou, E. Appert, A. Bocheux, S. Guillemin, F. Donatini, I. C. Robin, J. Kioseoglou and F. Robaut, *ACS Nano*, 2014, **8**, 4761-4770.
29. S. Guillemin, R. Parize, J. Carabetta, V. Cantelli, D. Albertini, B. Gautier, G. Bremond, D. D. Fong, H. Renevier and V. Consonni, *Nanotechnol.*, 2017, **28**, 10.

30. J. Zuniga-Perez, V. Consonni, L. Lymperakis, X. Kong, A. Trampert, S. Fernandez-Garrido, O. Brandt, H. Renevier, S. Keller, K. Hestroffer, M. R. Wagner, J. S. Reparaz, F. Akyol, S. Rajan, S. Rennesson, T. Palacios and G. Feuillet, *Appl. Phys. Rev.*, 2016, **3**, 100.
31. L. Lin, Y. F. Hu, C. Xu, Y. Zhang, R. Zhang, X. N. Wen and Z. L. Wang, *Nano Energy*, 2013, **2**, 75-81.
32. W. Deng, L. Jin, B. Zhang, Y. Chen, L. Mao, H. Zhang and W. Yang, *Nanoscale*, 2016, **8**, 16302-16306.
33. V. Consonni and A. M. Lord, *Nano Energy*, 2021, **83**, 105789.
34. S. Xu, Y. Wei, M. Kirkham, J. Liu, W. Mai, D. Davidovic, R. L. Snyder and Z. L. Wang, *J. Am. Chem. Soc.*, 2008, **130**, 14958-+.
35. J. Volk, T. Nagata, R. Erdelyi, I. Barsony, A. L. Toth, I. E. Lukacs, Z. Czigany, H. Tomimoto, Y. Shingaya and T. Chikyow, *Nanoscale Res. Lett.*, 2009, **4**, 699-704.
36. Y. G. Wei, W. Z. Wu, R. Guo, D. J. Yuan, S. M. Das and Z. L. Wang, *Nano Lett.*, 2010, **10**, 3414-3419.
37. J. J. Richardson, D. Estrada, S. P. DenBaars, C. J. Hawker and L. M. Campos, *J. Mater. Chem.*, 2011, **21**, 14417-14419.
38. K. Govender, D. S. Boyle, P. B. Kenway and P. O'Brien, *J. Mater. Chem.*, 2004, **14**, 2575-2591.
39. M. N. R. Ashfold, R. P. Doherty, N. G. Ndifor-Angwafor, D. J. Riley and Y. Sun, *Thin Solid Films*, 2007, **515**, 8679-8683.
40. J. J. Richardson and F. F. Lange, *Cryst. Growth Des.*, 2009, **9**, 2570-2575.
41. J. J. Cheng, S. M. Nicaise, K. K. Berggren and S. Gradečak, *Nano Lett.*, 2016, **16**, 753-759.
42. J. E. Boercker, J. B. Schmidt and E. S. Aydil, *Cryst. Growth Des.*, 2009, **9**, 2783-2789.
43. C. Lausecker, B. Salem, X. Baillin and V. Consonni, *J. Phys. Chem. C*, 2019, **123**, 29476-29483.
44. O. Cernohorsky, J. Grym, H. Faitova, N. Basinova, S. Kucerova, R. Yatskiv and J. Vesely, *Cryst. Growth Des.*, 2020, **20**, 3347-3357.
45. S. W. Chen and J. M. Wu, *Acta Mater.*, 2011, **59**, 841-847.
46. S. Guillemin, V. Consonni, E. Appert, E. Puyoo, L. Rapenne and H. Roussel, *J. Phys. Chem. C*, 2012, **116**, 25106-25111.
47. S. Guillemin, L. Rapenne, H. Roussel, E. Sarigiannidou, G. Bremond and V. Consonni, *J. Phys. Chem. C*, 2013, **117**, 20738-20745.
48. T. Cossuet, H. Roussel, J. M. Chauveau, O. Chaix-Pluchery, J. L. Thomassin, E. Appert and V. Consonni, *Nanotechnol.*, 2018, **29**, 11.
49. K. M. McPeak, M. A. Becker, N. G. Britton, H. Majidi, B. A. Bunker and J. B. Baxter, *Chem. Mater.*, 2010, **22**, 6162-6170.
50. K. M. McPeak, T. P. Le, N. G. Britton, Z. S. Nickolov, Y. A. Elabd and J. B. Baxter, *Langmuir*, 2011, **27**, 3672-3677.
51. A. Rodrigues, M. D. M. Alves and J. Morais, *Mater. Des.*, 2018, **142**, 240-246.
52. T. H. Hsieh, J. Y. Chen, C. W. Huang and W. W. Wu, *Chem. Mater.*, 2016, **28**, 4507-4511.
53. G. A. Chahine, N. Blanc, S. Arnaud, F. De Geuser, R. Guinebretière and N. Boudet, *Metals*, 2019, **9**, 352.
54. M. L. Foresti, A. Pozzi, M. Innocenti, G. Pezzatini, F. Loglio, E. Salvietti, A. Giusti, F. D'Anca, R. Felici and F. Borgatti, *Electrochim. Acta*, 2006, **51**, 5532-5539.
55. M. Wojdyr, *J. Appl. Crystallogr.*, 2010, **43**, 1126-1128.
56. D. Kashchiev and G. M. van Rosmalen, *Cryst. Res. Technol.*, 2003, **38**, 555-574.

57. R. Parize, J. Garnier, O. Chaix-Pluchery, C. Verrier, E. Appert and V. Consonni, *J. Phys. Chem. C*, 2016, **120**, 5242-5250.
58. V. Strano, R. G. Urso, M. Scuderi, K. O. Iwu, F. Simone, E. Ciliberto, C. Spinella and S. Mirabella, *J. Phys. Chem. C*, 2014, **118**, 28189-28195.
59. M. M. J. van Rijt, B. M. Oosterlaken, R. R. M. Joosten, L. E. A. Wijkhuijs, P. H. H. Bomans, H. Friedrich and G. de With, *Crystengcomm*, 2020, **22**, 5854-5861.
60. K. M. McPeak and J. B. Baxter, *Ind. Eng. Chem. Res.*, 2009, **48**, 5954-5961.
61. M. Q. Fatmi, T. S. Hofer, B. R. Randolf and B. M. Rode, *J. Chem. Phys.*, 2005, **123**, 054514.
62. S. P. Dagnall, D. N. Hague and A. D. C. Towl, *J. Chem. Soc. Faraday Trans. 2*, 1982, **78**, 2161-2167.
63. A. Kuzmin, S. Obst and J. Purans, *J. Phys.-Condens. Matter*, 1997, **9**, 10065-10078.
64. I. Persson, *Pure Appl. Chem.*, 2010, **82**, 1901-1917.
65. C. G. Tang, M. J. S. Spencer and A. S. Barnard, *Phys. Chem. Chem. Phys.*, 2014, **16**, 22139-22144.
66. M. Iachella, J. Cure, M. Djafari Rouhani, Y. Chabal, C. Rossi and A. Estève, *J. Phys. Chem. C*, 2018, **122**, 21861-21873.
67. S. Zhu, C. H. Su, S. L. Lehoczky, M. T. Harris, M. J. Callahan, P. McCarty and M. A. George, *J. Cryst. Growth*, 2000, **219**, 361-367.
68. T. Cossuet, E. Appert, J. L. Thomassin and V. Consonni, *Langmuir*, 2017, **33**, 6269-6279.
69. H. Li, L. Geelhaar, H. Riechert and C. Draxl, *Phys. Rev. Lett.*, 2015, **115**, 085503.
70. A. Sugunan, H. C. Warad, M. Boman and J. Dutta, *J. Sol-Gel Sci. Technol.*, 2006, **39**, 49-56.
71. M. Willander, O. Nur, Q. X. Zhao, L. L. Yang, M. Lorenz, B. Q. Cao, J. Z. Perez, C. Czekalla, G. Zimmermann, M. Grundmann, A. Bakin, A. Behrends, M. Al-Suleiman, A. El-Shaer, A. C. Mofor, B. Postels, A. Waag, N. Boukos, A. Travlos, H. S. Kwack, J. Guinard and D. L. Dang, *Nanotechnol.*, 2009, **20**, 40.
72. W. Tian, H. Lu and L. Li, *Nano Res.*, 2015, **8**, 382-405.
73. V. Consonni, J. Briscoe, E. Karber, X. Li and T. Cossuet, *Nanotechnol.*, 2019, **30**, 41.
74. Z. L. Wang, *Adv. Funct. Mater.*, 2008, **18**, 3553-3567.